Thermodynamics of Phase Transitions and Bipolar Filamentary Switching in Resistive Random-Access Memory

V. G. Karpov,[1] D. Niraula,[1] I. V. Karpov,[2] and R. Kotlyar[3]

[1] *Department of Physics and Astronomy, University of Toledo, Toledo, Ohio 43606, USA*
[2] *Components Research, Intel Corporation, Hillsboro, Oregon 97124, USA*
[3] *Process Technology Modeling, Intel Corporation, Hillsboro, Oregon 97124, USA*

(Received 4 February 2017; revised manuscript received 22 April 2017; published 30 August 2017)

We present a phenomenological theory of bipolar filamentary resistive random-access memory describing the commonly observed features of their current-voltage characteristics. Our approach follows the approach of a thermodynamic theory developed earlier for chalcogenide memory and threshold switches and largely independent of their microscopic details. It explains, without adjustable parameters, such features as the domains of filament formation and switching, voltage-independent current in SET and current-independent voltage in RESET regimes, the relation between the set and reset voltages, filament resistance independent of its length, etc. Furthermore, it expresses the observed features through the material and circuitry parameters, thus paving the way to device improvements.

DOI: 10.1103/PhysRevApplied.8.024028

I. INTRODUCTION: QUESTIONS

Filamentary resistive random-access memory (RRAM) devices have been a subject of intensive investigations for more than a decade. In spite of a significant amount of data accumulated for various materials systems, many aspects of device operations are not understood and, unlike, e.g., spin-transfer-torque memory [1], their understanding remains rather limited, and a sufficient theory of the resistive-switching phenomena is not yet available.

There is a consensus about the crucial role of conductive filaments (CFs) determining RRAM operations. CFs can break switching the device into the RESET state. Reestablishing CF would switch the system into its SET state. The existing models of CFs are either qualitative or entirely numerical, containing a number of adjustable parameters.

This work introduces a quantitative phenomenological theory of RRAM answering several outstanding questions. They are listed in Table I referring to the sketch of typical current-voltage characteristics in Fig. 1. As an example, we elucidate the symmetry $U_{\rm RESET} = -U_{\rm SET}$, similarity between $U_{\rm RESET}$ and $U_{\rm SET}$ in various systems, vertical and horizontal domains of the current-voltage characteristics in the SET and RESET regions, respectively, etc.

Our theory below provides quantitative answers to the questions of Table I in the framework of a phenomenological analysis that does not specify the microscopic structure of CFs or the details of chemical composition. Instead, it concentrates on generic thermodynamic properties consistent with the data. The quantitative description is achieved by introducing the chemical potentials of different phase states involved and considering the system free energy that includes the thermal, the electric, and the chemical components.

The consideration is organized as follows. It starts with a purely qualitative discussion in Sec. II that explains without any math the model and the logic of the paper; that section is appropriate because the paper deals with a variety of subjects formally belonging to different fields in physics and applications. In Sec. III, we introduce our model of CFs with a previously overlooked property of the polarity-dependent electric charging. Section IV describes the thermodynamic analyses of nucleation and growth processes related to the domains in Fig. 1 and Table I. These processes are treated quantitatively in Sec. V.

II. QUALITATIVE DESCRIPTION

Here, we present a low-resolution "bird's-eye" view guide through subsequent consideration, some parts of which contain the inevitable distracting details. This section provides a brief summary of this paper's approaches and major results.

(1) In Sec. III, we describe a model independent capacitive property of CFs, i.e., its ability to accumulate electric charges in response to the applied bias. The charges generate strong lateral electric fields polarizing the existing electric dipoles and/or creating the displacements of charged defects in the surrounding host, which couples CFs with the insulating matrix. That coupling is bias dependent, thus explaining the nature of SET and RESET transitions under biases of opposite polarities.

(2) Also, in Sec. III, we show how the latter polarization becomes possible at temperatures exceeding a certain freezing temperature (qualitatively similar to the glass transition temperature), which is determined by the applied voltage and its pulse width or ramping rate. The same freezing temperature determining the SET and RESET transitions makes their corresponding voltages equal in absolute value.

 © 2017 American Physical Society

TABLE I. Outstanding questions about RRAM current-voltage (I-U) characteristics.

Domain marked in Fig. 1[1,b]	Question
A-B, switching at threshold voltage U_T.	What is the nature of the snapback at U_T and its dependence on material and circuit parameters, temperature, and voltage rate?
B-C, vertical I-U curve at U_{SET}.	U_{SET} vs material parameters.
C-0-D, the *on*-state (low-resistance) domain.	Filament radius and resistance $R \propto 1/I_{\text{SET}}$ vs material parameters.
D-E, switching to R_{RESET} at U_{RESET}.	Why does the resistance increase past U_{RESET}? What is the nature of snap forward? Expression for U_{RESET}, I_{RESET}, and snap-forward ratio I_D/I_E.
E-F, the current saturating to $I_{R,\text{sat}}$ or slightly increasing towards U_{STOP} ("horizontal I-U curve").	Expressions for $I_{R,\text{sat}}$ and/or $I(U)$ in E-F.

[a]Here, we limit ourselves to the case of bipolar RRAM undergone during the filament-forming process.
[b]We do not discuss here the *off*-state (high-resistance) domain F-0-A, in which I-U characteristics are determined by the insulating material properties without structural transformations.

(3) In Sec. IV, we show that a sufficient description of the empirically observed RRAM facts requires that the material involved has at least three distinct phases: stable insulating, metastable conductive, and unstable conductive. Also, we analyze the role of material amorphicity and related observations of logarithmic time relaxations, noises, and parameter drifts.

FIG. 1. A sketch of the typical current-voltage characteristics [2–7] showing various domains in Table I. U is the voltage across the device, which is different from the power source voltage V due to the load resistor R_L effect. In particular, the latter can change the shape of the A-B and B-C domains decreasing the difference between U_T and U_{SET}; subtracting the voltage drop across R_L leads to a noticeable difference between U_{T} and U_{SET} [2–4]. U_{STOP} is determined by the maximum absolute value of voltage V during the reset process. The slope R at point C is the conductive-filament resistance. Note that, in experiments, the SET current I_{SET} is defined as the maximum (compliance) current allowed. The dashed fragment in the third quadrant shows the sometime-observed deviations from the current saturation behavior with $|I_F| \gtrsim |I_E|$. The dashed fragment in the first quadrant represents the switching part of the SET process where the data points between A and B may not be measurable.

(4) Based on the latter three-phase diagram, the quantitative analyses of SET and RESET processes in Sec. IV separately addresses the nucleation and growth processes, including the nucleation of CFs and its radial growth, as well as the nucleation and growth of insulating gap responsible for the high resistive state. We derive analytical results for the threshold-switching voltage, CF radius, SET voltage, the RESET current drop, the gap width, and the saturated RESET current through the material parameters.

III. FILAMENT MODEL

Any CF model has to address a significant fact: that CF resistance is practically independent of its length h. An often-assumed picture of CFs postulates a local geometrical constriction responsible for CF resistance (the hourglass model [8,9]). In that model, the RESET and SET processes are attributed to the destruction and restoration of the constriction. Experimentally, it was found that CFs can have a truncated cone shape. However, the radii of that cone faces are typically different by only a numerical factor [10,11], $r_1/r_2 \sim 2$, not significant enough to attribute the entire cone resistance to its narrow region [the truncated cone resistance [12], $R_{\text{cone}} = \rho h/(\pi r_1 r_2)$, where ρ is the resistivity and h is the filament length].

A. Filament electrostatics

Our phenomenological theory below does not specify CF structure, treating it as a formed conductive cylinder; we will not assume that its conical shape is essential. The CF resistance independent of its length h will be explained without the assumption of its determining constriction [see Eqs. (33) and (35)]. As an alternative structure-independent feature, our model in Fig. 2 includes the electric charges accumulated by CFs due to its electric capacitance, as explained next; they induce electric polarization that couples the host and the CF.

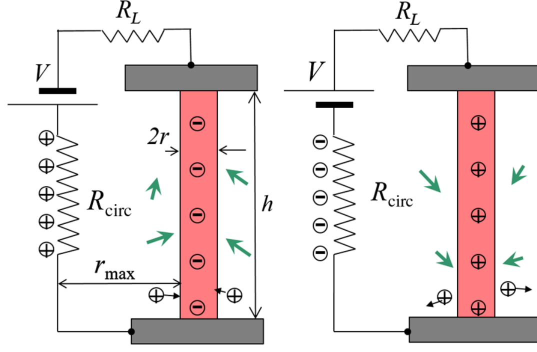

FIG. 2. A conductive filament under biases of different polarities accumulates the electric charges (denoted by ⊖ and ⊕), creating the electric field that (left panel) attracts or (right panel) repels ions (for the specificity shown as ⊕ outside the filament). R_{circ} represents the system wires with their own capacitance and charges, characterized by the linear dimension r_{max}. R_L is the load resistance; $R_L \gg R_{circ}$. Short arrows represent the electric polarization along the energetically favorable directions parallel to the local field.

The latter polarization can be caused by either redistribution of ions or reorientation of local embedded dipoles. The existence of such dipoles does not necessarily imply that the host material exhibits bulk ferroelectricity. It is indeed known that making HfO_2 ferroelectric requires particular doping and growth techniques stabilizing the nonequilibrium orthorhombic phase [13]. However, strong-enough electric dipoles with high susceptibility can exist locally due to the stress- or field-related conditions around CFs. They were observed even for amorphous morphologies [14] and can be vitally important for the understanding of materials with high dielectric permittivity [15], such as HfO_2. For a particular case of Hf-based RRAM, it should be noted that the high dielectric permittivity $\varepsilon \approx 25$ is mostly due to ionic displacements [16] [as follows from a comparison with the square of the refraction index (approximately 2.1)] and can be pinned by some defects.

1. Filament charging

To describe CF charging, we recall the well-known model of two long parallel wires of radius r and resistance R, each separated by a distance $r_{max} \gg r$ and connected to the power source through resistance $R_L \gg R$. The potentials of the wires will be different by IR_L. The latter potential difference results in capacitive linear charges $\pm\beta$ on the wires. The linear charge density β is found by equating the integral of its created electric field $2\beta/r$ to IR_L. As a result, the capacitance (C) and charge (β) per length and the radial electric field at the wire surface (E_r) become (in Gaussian units)

$$C = \left[2\ln\left(\frac{r_{max}}{r}\right)\right]^{-1}, \qquad \beta = IR_L C, \qquad E_r = \frac{2\beta}{r}, \quad (1)$$

where I is the current. Because $r_{max} \gg r$, changing r_{max} by a numerical factor or even by an order of magnitude (say, from 1 mm to 1 cm) will not significantly change the results in Eq. (1), which are not sensitive to the circuitry design. The expression for linear charge density β reflects its capacitive nature corresponding to the voltage difference IR_L between CFs and the rest of circuitry separated by the load resistance.

A simple analysis leading to Eq. (1) can be related to Fig. 2 by identifying one of the two parallel wires to CFs and another to the lump circuit resistance R_{circ}. The fact that the second wire may not be parallel to the CF is of no importance due to the inequality $r_{max} \gg r$, as noted after Eq. (1). The constraint $R_L \gg R$, R_{circ} is not significant and can be relaxed, as explained in the rest of this subsection below.

The phenomenon of electric fields produced by current-carrying wires has been known since 1852, first considered by Weber, as is thoroughly discussed in Ref. [17]. (We note parenthetically that, with rare exceptions [18], it is not sufficiently presented in the standard physics curricula, being overshadowed by the magnetic phenomena caused by electric currents.) Specifically, the expression for E_r can be derived without the above assumption of $R_L \gg R$ [Eq. (6.21) in Ref. [17]], making E_r dependent on the longitudinal coordinate z measured from the wire midpoint,

$$E_r = \frac{1}{r}\left[\ln\left(\frac{r_{max}}{r}\right)\right]^{-1}\left[IR_L + \frac{IR}{2}\left(1 - \frac{2z}{h}\right)\right]. \qquad (2)$$

We observe that the radial field around the CF remains proportional to the current I, and its direction is determined by the current polarity. Equation (2) describes the circuitry in Fig. 2 when R_{circ} is included in the load resistance: $R_L \to R_L + R_{circ}$ in Eq. (2).

The generalization in Eq. (2) shows that the effect of filament charging and its based analysis below remains, regardless of the load-resistor value. One other observation is that the radial field effects exist for either sign of I. That field and polarization directions are determined in the process of device electroforming (by the sign of the forming voltage pulse [19]). Therefore, in this theory framework, RRAM can be formed and operated by bias of any polarity, which is consistent with the body of various experimental data.

Finally, we note that when the surrounding material polarization Π is aligned with the electric field E_r, its related energy density $-\Pi E_r$ does not change sign with z [as opposed to E_r in Eq. (2)] and remains significantly negative relative to the energy gain. In the opposite case of antialigned Π (achievable by fast switching of the current polarity), the energy density is positive, corresponding to the energy loss conducive to CF breakup, as explained in what follows.

2. Filament screening

A realistic analysis takes into account that a CF-induced lateral field must be screened by the redistribution of free electrons in the metal electrodes. Such a screening of a charged filament was considered in Ref. [20]. It was shown that CF-induced lateral electric field is screened at distances of the order of filament length h, which is intuitively clear from the image-charge argument. As a result, $r_{\max}$ under the logarithm in Eq. (1) should be replaced with h, which makes the radial electric field fully independent of a particular circuit design.

To avoid any misunderstanding, we note that the latter electrode screening takes place for the equipotential electrodes, each at its own potential; the potential difference between the electrodes equals the applied voltage. In fact, it is the screening that maintains the electrode equipotentiality by eliminating the tangential component of the electric field at the electrode interfaces.

While the filament capacitance is numerically insignificant—say, $C \sim 0.1$ pF/cm—its radial electric field is strong due to the relatively small radius $r \ll h$. The field in Eq. (1) is strong compared to the longitudinal field IR_L/h between the electrodes, with the ratio $E_r/E = (h/r)/\ln(h/r) \gg 1$ (that remarkable strength of the radial electric field was noticed also in Ref. [17]).

3. Other considerations

C in Eq. (1) should not be mixed with the specific capacitance of a stand-alone thin metal needle analyzed since Maxwell [21–23], and given, per length, by

$$C_0 = \left[2\ln\left(\frac{h}{r}\right)\right]^{-1}, \quad (3)$$

numerically close to C. The difference between the C and C_0 effects is that the former accumulate capacitive charges due to the electric-current-caused potential difference, which depends on the current polarity, while the latter acquires charges in response to the chemical-potential difference between the material of the CF and its surrounding material; i.e., it is polarity independent. (Theoretically, applying external bias between the two phases would introduce the electrochemical potential instead of the chemical one making the effect polarity dependent as well; however, it is not quite clear how such a bias could be introduced.) For example, estimating the Fermi-energy difference between a Hf-dominated CF and its surrounding HfO_2 [24] as $\delta E_F \sim 1$ to 2 eV, the current-independent charge per length becomes

$$\beta_0 = \frac{C_0 \delta E_F}{e}, \quad (4)$$

where e is the elemental charge. Depending on the relation between β and β_0, one can predict current-I-driven changes in the electric field E_r contributing to CF-related operations in both bipolar and unipolar modes.

Through the radial electric field, the bias polarity will stimulate redox or other processes affecting CF size and morphology. Specifically, the above-predicted electric field E_r could explain the radial drift of ions assumed by the ion-drift models for RRAM operations (see, e.g., Ref. [25] and the references therein). However, our phenomenological treatment here does not explicitly specify the underlying microscopic models.

Equation (1) formally predicts a CF-generated radial electric field that should disappear when the current is turned off, $I = 0$. In Sec. IV below, we consider the atomic rearrangements (ion or ferrodisplacement) electric polarization $\mathbf{\Pi}$ caused by that field. Such a polarization possesses significant inertia, making it long-lived after the current is turned off. Furthermore, we will show that a self-consistent state of CF charge and surrounding polarization can form a polaronlike stable or metastable state.

B. Freezing temperature

Another model-independent statement pertains to the fact that a CF does not undergo any significant changes (representing a long-lived conductive channel) when the voltage across the device is between U_{SET} and U_{RESET}, while voltages beyond that interval cause significant CF transformations. Specifically, $R = dV/dI$ determines the resistance of the long-lived CF that does not change between U_{SET} and U_{RESET}, i.e.,

$$R(U_{\mathrm{SET}}) = R(U_{\mathrm{RESET}}). \quad (5)$$

Phenomenologically, the property of U_{SET} and U_{RESET} to confine the regime of CF stability means that they play the role of “freezing” or “unfreezing” voltages, such that the temperature above U_{SET} and below U_{RESET} must be higher than some freezing temperature T_f, while it is below T_f when $U_{\mathrm{RESET}} < U < U_{\mathrm{SET}}$. T_f can correspond to a particular phase transition, such as, e.g., glass transition [26], but also, in general, to any thermally activated process. Assuming the activated atomic transformation with the characteristic time $\tau_0 \exp(-W_a/kT)$, where $\tau_0 \sim 10^{-13}$ s is the characteristic period of atomic vibrations, k is the Boltzmann’s constant, and W_a is the activation energy. T_f is determined by the condition (similar to Refs. [26–28])

$$\tau_p = \tau_0 \exp(W_a/kT_f), \quad (6)$$

where τ_p represents the voltage pulse width or $[d(\ln U)/dt]^{-1}$ for a continuously varying voltage $U(t)$.

The Joule-heat-related temperature change is described by $\delta T = T_f - T_0 = \tau_T P/kN_a$, where τ_T is the thermalization time, T_0 is the room temperature, $P = U^2/R$, and N_a is the number of degrees of freedom (roughly equal to the number of atoms) in the region involved. Therefore, the freezing or unfreezing condition takes the form

TABLE II. Processes and chemical potentials corresponding to different domains in Fig. 1.

Domain	Process	CP[a]
A-B	Nucleation and longitudinal growth of a narrow unstable CF shorting between the electrodes	$\mu_{\rm uc} = \mu_i + \delta\mu_1 > \mu_i$
B-C	Radial growth of the long-lived charged CF and its stabilizing polarization near point C, making CF long-lived	$\mu_{\rm uc} \to \mu_{\rm mc} = \mu_{\rm uc} - \delta\mu_2 < \mu_{\rm uc}$, $\mu_{\rm mc} > \mu_i$
C-0-D	Long-lived metastable CF changing the charge polarity at point 0	$\mu_{\rm mc}$
D-E	Unfreezing oppositely charged metastable CF in the “wrong polarization” environment, CF breakup via nucleation of insulating gap	$\mu_{\rm mc} \to \mu_i$
E-F	Increase in the insulating gap to its steady-state width	μ_i

[a]CP stands for the chemical potentials of the insulating phase (μ_i), unstable CF ($\mu_{\rm uc}$), and metastable CF ($\mu_{\rm mc}$) phases illustrated in Fig. 3.

$$\tau_T \frac{U^2}{RN_a} = \frac{W_a}{\ln(\tau/\tau_0)} - kT_0. \tag{7}$$

Since the criterion in Eq. (7) is satisfied for voltages $U_{\rm SET}$ and $R(U_{\rm SET}) = R(U_{\rm RESET})$ according to Eq. (5), we conclude that it is satisfied when $U_{\rm RESET} = -U_{\rm SET}$, thus elucidating the latter relation pointed out among the outstanding challenges in Table I. We note that our model does not rely on details of any particular microscopic mechanism for Eq. (7) unlike, say, Eqs. (1)–(6) in Ref. [25]. In particular, it remains applicable to the processes in glasses of phase-change memory where bipolar switching was recently observed [29].

Furthermore, Eq. (7) predicts that $U_{\rm SET}$ and $U_{\rm RESET}$ will change logarithmically with τ_p, which was observed [2,30–32]. We note that, in a noncrystalline system, the activation energies generally vary between different local regions in the manner described in Sec. IV C.

IV. CHEMICAL POTENTIALS

A. Three states of the system

Similar to the standard phase transitions, we assume CF transformation through the nucleation and growth stages. The newly nucleated phases may not be immediately stable or even long-lived. We consider a possibility that they initially appear to be unstable, having to undergo further transformations towards stability. Indeed, it was independently argued [33] that in polymorphic systems, nucleation can evolve in two steps, through an intermediate metastable phase. Also, it has been experimentally observed that CFs can be annealed at a high-enough temperature [34,35]; i.e., it presents a metastable state long-lived enough to have practical significance as a nonvolatile memory.

Table II specifies our model processes and their corresponding chemical potentials related to various domains in Fig. 1. The field-induced nucleation at the threshold voltage U_T is followed by the longitudinal growth of a narrow CF that is unstable without the electric field. As shown below, its subsequent radial growth is characterized by resistance R inversely proportional to the current—and hence the vertical current-voltage characteristic at $U_{\rm SET}$. The chemical potential of the structure constituting that unstable CF is higher than that of the insulating host, $\mu_{\rm uc} > \mu_i$, as reflected in Table II.

The relations between the chemical potentials of insulating, unstable (short-lived) conductive, and metastable (long-lived) conductive phases and their corresponding thermodynamic barriers are illustrated in Fig. 3 for zero electric field, and in Fig. 4 for finite electric biases in RRAM operation. The barriers describe energetically unfavorable configurations through which the system evolves towards a metastable or stable state.

While energetically most favorable under zero bias [Fig. 4(a)], the insulating phase significantly increases its

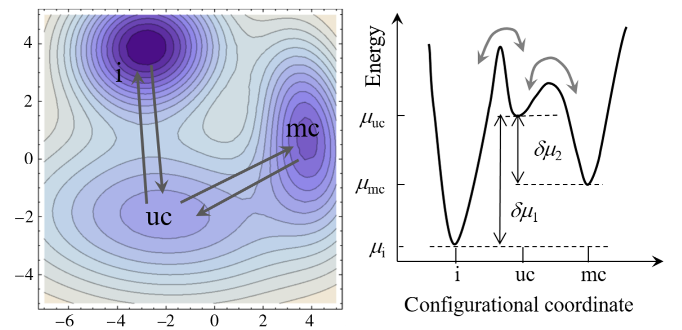

FIG. 3. (Left panel) A contour plot of the system chemical potentials in 2D space of unspecified configurational coordinates showing three distinct minima corresponding to the insulating (i), unstable conductive (uc), and metastable conductive (mc) phases and their related barriers. (Right panel) 1D presentation of the same along an unspecified coordinate. Arrows represent transformations between the mc and uc and the uc and i phases where the energy barriers are relatively low.

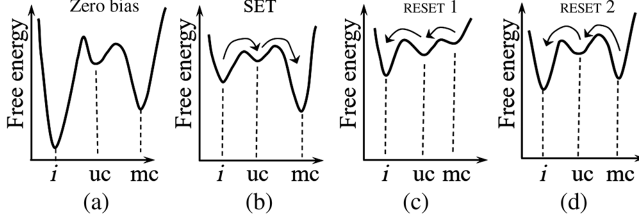

FIG. 4. Free energy vs configurational coordinate under different electric biases corresponding to Fig. 1. (a) Zero bias (same shape as in Fig. 3). (b) Point A, bias U_T triggering a SET process by nucleation and radial growth of the CF. (c) Point D, the opposite polarity charge triggering RESET via CF breakdown by nucleation of the insulating gap. (d) Point E, a strong field and a composite CF combining an insulating gap and conductive domains in the final stage of RESET. See the text for further details.

energy ($\propto E^2$) under electric bias due to the strong electric field, $E = U/h$. Assuming, as usual, a load resistance R_L in series with the device resistance R, the source voltage V corresponds to the device voltage $U = VR/(R + R_L)$ considerably lowered by CF that introduces a low-resistance R path. Therefore, under electric bias, the conductive states have lower energy than the insulating one, as reflected in Fig. 4(b). In the same diagram, arrows show the processes of nucleation and growth through a short-lived state (uc), with the left barrier playing the role of nucleation barrier decreased by the field, as described in Sec. V A 1. The latter short-lived state then decays into the long-lived conductive state (mc), which is lower in energy than the insulating state (i); this sequence constitutes the SET process.

Presented in Fig. 4(c) is the system with SET-formed CF under the instantaneously reverted bias polarity. The inherited polarization conflicting with the instantaneously acquired CF opposite charge strongly increases the free energy of a formerly stabilized CF state, making it unstable and triggering CF breakdown by forming an insulating gap. This constitutes the first stage of the RESET process, which is described more quantitatively in Sec. V A 2.

Shortly after CF polarity reversal, the surrounding polarization realigns correspondingly, lowering CF energy as depicted in Fig. 4(d). The subsequent growth of the insulating gap proceeds through the energetically unfavorable short-lived (uc) state represented by arrows in Fig. 4(d). This constitutes the second stage of RESET quantitatively described in Sec. V B 2.

Phenomenologically, $\delta\mu_1 = \mu_{uc} - \mu_i$ remains a material parameter. It can be estimated for specific CF models, such as those formed by oxygen vacancies in HfO_2. Assuming their relative concentrations in the bulk and CF to be, respectively, $n_b \sim 0.1$ and $n_{CF} \sim 1$, and using the results for dilute solutions ($n_b \ll 1$) [36], one gets

$$\delta\mu_1 = \frac{kT}{a_0^3}\ln(n_{CF}/n_b), \tag{8}$$

where a_0^3 is the volume per vacancy, roughly equal to the atomic volume. Based on the temperature measurements [37], we take $T \sim 600$ K. Taking $a_0 \sim 0.2$ nm as well yields $\delta\mu_1 \sim 10^9$ J/m^3.

At a certain radius and resistance satisfying the criterion in Eq. (7) with $U = U_{SET}$, CF becomes stabilized by the host polarization, as explained in Sec. III before the paragraph containing Eq. (1). Its structure remains frozen in the interval of voltages $U_{RESET} < U < U_{SET}$. The polarization Π contribution to the chemical potential is given by [38] $\delta\mu_2 = \mathbf{\Pi}\cdot\mathbf{E}$ where $\mathbf{E}$ is the electric field, which is due to the charged CF for the case under consideration.

We describe the polarization assuming that it significantly screens the filament field, i.e., $\mathbf{E} \approx -4\pi\Pi$, and

$$\delta\mu_2 = |E\Pi| \approx 4\pi\Pi^2. \tag{9}$$

According to definition, the polarization $\Pi = (ea)n$, where ea is the elemental dipole corresponding to the elemental (ion) charge e shifted over distance a, and n is the concentration of such dipoles. We take the typical $a \sim 0.1$ nm, and $n \sim 10^{22}$ cm^{-3}, which yields $\delta\mu_2 \sim 10^9$ J/m^3. In spite of the order-of-magnitude coincidence, $\delta\mu_1 \sim \delta\mu_2$, one should assume $\delta\mu_1 > \delta\mu_2$, on empirical grounds reflected in Table II. Note that the above estimated polarization does not require a significant diffusion of ions in the host material and thus can be fast enough to explain the observed fast transformations.

With voltage U across the device changing its polarity, so does the electric charge density β on the CF, and its corresponding electric field $\mathbf{E}$. Therefore, the former polarization becomes energetically unfavorable, leading to the chemical potential $\mu_{mc} + |\mathbf{\Pi}\cdot\mathbf{E}| > \mu_{mc}$ and triggering CF disruption at U_{RESET}, when the criterion in Eq. (7) is satisfied and CF structure thaws off. The disruption creates an insulating gap, which can grow further, as described in Secs. V A 2 and V B 2.

Finally, we note that a three-phase model similar to that of Fig. 3 can be developed for the alternative case when the chemical potential of conductive phase is the lowest, as, for example, takes place in the phase-change memory structures. Indeed, it was observed that the structural transformations in phase-change memory involve more than just two phases [39]; hence, a three-phase description is relevant.

B. Bound states of CF charge and polarization

In connection with the concept of a polarization-stabilized CF, we would like to point out the possibility of the polaronlike bound states retaining the CF charges even after the current I [in Eq. (1)] is turned off. Indeed, based on the standard thermodynamics of dielectrics, the polarization-energy gain can be represented as [38]

$$\delta F = -\frac{h}{2}\int_r^h \Pi E_r(r')2\pi r' dr' = (1-\varepsilon)h\beta^2 \ln\left(\frac{h}{r}\right), \quad (10)$$

where we have taken into account that $\Pi = E_r(\varepsilon - 1)/4\pi$.

One can analyze the possibility of persistent CF charging by adding to Eq. (10) the energy-loss terms βhV and $(\beta h)^2/2(Ch)$, with β and C taken from Eq. (1). They present, respectively, the work done to move the electric charge through the voltage source V and to charge the CF capacitor. Approximating $V \approx IR_L$, it is straightforward to see that persistent CF charging is energetically favorable if $\varepsilon > 2 + \ln(h/r)$. The latter condition takes place for high-dielectric-permittivity materials. More-realistic estimates should include the polarization-related anisotropy, strains, and nonlinearity.

C. Role of amorphicity

Here, we discuss the role of the amorphicity of the material phases involved. It is well known, from the physics of amorphous materials, that they are nonequilibrium systems gradually decreasing their energies with time (aging). Specifically (see Ref. [40] and the references therein), the amorphous structure relaxation processes are responsible for the observed drift of parameters in phase-change memory based on chalcogenide glasses.

The atomic configurations undergoing structural transformations are described as double-well atomic potentials characterized by the random thermodynamic barriers W_B. The probabilistic distribution of the random barriers W_B is approximated as uniform,

$$g(W_B) \approx 1/\Delta W_B, \qquad \Delta W_B = W_{B,\max} - W_{B,\min}, \quad (11)$$

between the two boundary values. That makes their relaxation-time distribution reciprocal in t, and its related change in the system energy is logarithmic in time [40],

$$\delta\mu = \delta\mu_{\min} + (\delta\mu_{\max} - \delta\mu_{\min})f(t), \quad (12)$$

where the distribution function of relaxation times is given by

$$f(t) = \frac{kT}{\Delta W_B}\ln\left(\frac{t}{\tau_{\min}}\right), \qquad \tau_{\min} < t < \tau_{\max}, \quad (13)$$

and

$$\tau_{\max(\min)} = \tau_0 \exp(W_{B,\max(\min)}/kT). \quad (14)$$

$f(t)$ saturates at $f_{\max} \equiv f(\tau_{\max}) = 1$ for times $t > \tau_{\max}$ and can describe a remarkably broad time interval ranging from $\tau_{\min}$ shorter than one microsecond to, say, $\tau_{\max} \sim 10^5$ s, assuming $\tau_0 \sim 10^{-13}$ s (a characteristic atomic-vibration time) and $W_{B,\max} = 1$ eV as a rough estimate.

According to Eqs. (12) and (13), any structural transformation in Table II and Fig. 3 involving one or more amorphous components will exhibit long time-relaxation behavior following logarithmic dependence. In some cases, these underlying logarithmic dependencies reveal themselves in other temporal forms entering results in exponents or other functions, such as, e.g., the temporal drift of resistance [40] given by

$$R(t) = R(0)\left(\frac{t}{\tau_{\min}}\right)^{\nu}, \qquad \nu = \frac{Du_0}{\Delta W_B}, \quad (15)$$

where D is the deformation potential and u_0 is the saturated value of the relative volume change (dilation), so that $\nu \sim 0.03$. The underlying mechanism is the material deformation changing the Fermi energy and resistance.

Long time logarithmic-type relaxations in RRAM devices have been observed [2,30,31]. Still more evidence of random double-well atomic potentials is the $1/f$ noise [41] (see details in Sec. VIII.3.3 of Ref. [42]). $1/f$ noise corresponds to the self-correlation function (also known as the Pearson correlation coefficient) logarithmically decaying with time [43]. Therefore, the recently observed [44] correlation coefficient decaying linearly in $\log t$ for RRAM resistance measurements separated by time t can be related to the above-described random double-well potentials.

The latter assertion requires a special comment explaining how the measurements in RRAM devices reveal mostly the random telegraph noises (RTNs; see Refs. [45,46] and the references therein) rather the $1/f$ noise. RTNs are commonly related to double-state fluctuators (double-well potentials) when the number of such fluctuators is small [42]. When the size of large systems with $1/f$ nose decreases to a degree where there are only a few fluctuators left, the noise acquires the behavior of the RTN. Conversely, the superposition of a great number of two-state fluctuators corresponding to small devices with various relaxation times is seen as $1/f$ noise [47,48].

The latter argument applies to RRAM filamentary devices where the effective volume contributing to operations is extremely small, limited to a fraction of the CFs undergoing structural transformations; similarly small is the number of contributing fluctuators corresponding to noises of not-too-low frequencies and revealing themselves via RTN signal. However, in extremely long time measurements, the number of significant fluctuators increases to include those with lengthy relaxation times. A system with a large number of fluctuators possesses $1/f$ noise behavior, which explains the observed logarithmic decay of correlation functions [44].

It is a general feature specific of the RRAM nanosized devices that the number of double-well potentials affecting CFs is rather limited, i.e., not much larger than unity. Therefore, the results of the reprograming of a given device cannot be accurately described by averaging over

continuous distribution of barriers characterizing the corresponding infinite system. This new situation of "nanoglass" remains to be further explored, although some important results are listed in Sec. V.3 of Ref. [42]. Here, we limit ourselves to stating that the lack of self-averaging in a small system with random double-well potentials leads to significant variations in their created deformations [49], and thus resistances, some of which will increase or decrease in the course of reprograming. This type of behavior was observed with the magnitude of dispersion increasing towards small-radius CF devices [2].

Also, we would like to point out the data on resistance variations as a function of the number of device reprograming cycles N [Fig. 3(a) of Ref. [50]] exhibiting the dependence $R \propto N^{\nu}$ for both high- and low-resistance states. In the meantime, this or another specific device exhibits noticeable fluctuations between programing cycles.

We speculate that the latter dependence can be explained by Eq. (15), where t is replaced with N. Such an interpretation implies that increasing the number of reprograming cycles increases the total time of exposure to elevated temperatures activating higher and higher barriers in the system. While this is not the standard temporal drift of parameters of a stand-alone device, it can be described as the "reprograming parameter drift".

Finally, we would like to point out a difference between the temporal dependencies in Eq. (12) and those of Eq. (7). The behavior in Eq. (12) is due to multiple random activation barriers in a broad interval of energies, characteristic of amorphous systems. On the contrary, Eq. (7) describes a time dependence in a system with a single energy barrier W_a. Specifically, it shows how a power of perturbation, necessary to change the material structure, depends on the time during which it is exerted, while Eq. (12) predicts long time relaxations that are independent of the power injected.

V. QUANTITATIVE ANALYSIS

A. Nucleation events

Here, we consider the two nucleation events alongside the other processes listed in Table II.

1. Threshold switching

Our thermodynamic approach relates the threshold voltage U_T to the field-induced nucleation [51–54]. Omitting the details, it can be presented, in Gaussian units, as [from, e.g., Eq. (13) of Ref. [51] and with the additional multiplier 1/2 derived in Ref. [55]]

$$U_T = \frac{hW_0}{kT\ln(\tau_p/\tau_0)}\sqrt{\frac{3\pi^3\alpha^3\Lambda W_0}{32\varepsilon r_c^3}}, \tag{16}$$

where

$$W_0 = 16\pi\sigma^3/3\delta\mu^2 \quad \text{and} \quad r_c = 2\sigma/\delta\mu$$

are the classical nucleation barrier and radius [56], σ and $\delta\mu$ are the interfacial tension and the difference in chemical potentials between the insulating host and the CF, $\alpha = r_{\min}/r_c \sim 0.1$, $r_{\min}$ is the minimum CF radius (consistent with its integrity), ε is the dielectric permittivity of the host material, τ_p is the electric pulse length, and $\tau_0 \sim 10^{-13}$ s is the characteristic atomic-vibration time in solids; $\Lambda \lesssim 10$ is a multiplier logarithmically dependent on the embryo aspect ratio.

Equation (16) is convenient for estimates because the characteristic ranges of $W_0 \sim 1$–3 eV and $r_c \sim 1$–10 nm are known for various cases of nucleation in solids [57–65]. We note that, corresponding to the abovementioned ranges for W and r_c, our results predict a broad range of threshold voltages from 0.2 to 5 V that can explain multiple observations for different systems. Here, we use $r_c \sim 3$ nm and $W_0 \sim 3$ eV. Setting also $h \sim 10$ nm, $\ln(\tau_p/\tau_0) \sim 10$, $\varepsilon \sim 25$, and $T \sim 600$ K (due to the Joule heat [19]) yields $U_T \sim 1$ V, consistent with the typical data [66].

We recall that the mechanism of field-induced nucleation [51–54] is based on a strong reduction of the electric-field energy due to nucleation of a conductive-needle-shaped embryo. Once created, the field strength is further amplified towards its tip (the lightning-rod effect). Therefore, nucleation of the next embryos at the tip becomes easier, and the probability of formation of a narrow CF is determined by the first nucleation event at the threshold voltage given in Eq. (16). The radial growth of a just-formed narrow CF with $r \sim r_{\min}$ is described in Sec. V B 1.

Note that the above description defines the threshold voltage through the condition

$$\tau_p = \tau_0 \exp\left(\frac{\tilde{U}}{U}\right) \quad \text{when } U = U_T, \tag{17}$$

where $\tilde{U}$ is presented by an obvious combination of parameters from Eq. (16), for example,

$$\tilde{U} = \frac{hW_0}{kT}\sqrt{\frac{3\pi^3\alpha^3\Lambda W_0}{32\varepsilon r_c^3}}. \tag{18}$$

If the field increases with time, so that $U = \lambda t$ (used in some experimental studies), then the probability p of nucleation is described by the equation

$$\frac{dp}{dt} = \frac{1}{\tau_0}\exp\left(-\frac{\tilde{U}}{U}\right). \tag{19}$$

Integrating the latter and setting $p = 1$ defines the threshold voltage through the equation

$$U_T \approx \tilde{U}\left[\ln\left(\frac{U_T^2}{\lambda\tilde{U}\tau_0}\right)\right]^{-1}. \qquad (20)$$

The transcendental equation (20) can be easily iterated by replacing U_T under the logarithm with its approximate value starting with $U_T = \tilde{U}$, leading to

$$U_T \approx \tilde{U}\left[\ln\left(\frac{\tilde{U}}{\lambda\tau_0}\right)\right]^{-1}, \qquad (21)$$

etc., where Eq. (21) provides a rather close approximation with an accuracy of approximately 10%. It predicts that U_T should increase with the sweep rate λ, which is consistent with the data.

Another aspect of nucleation switching important for noncrystalline nanodevices is its stochastic nature. It was shown [52,53] that, because of the inherent disorder, the delay times of switching and the threshold voltages are statistically distributed and the width of these statistical distributions decreases with the area of a structure (i.e., a CF cross section) where the nucleation takes place. Conversely, the increase in U_T variations is due to suppression of self-averaging with the area decrease. The underlying physics is that the field-induced nucleation in a RRAM structure takes place through the gap of the preliminary formed filament, whose cross-section area is rather small (on the order of several nanometers). Therefore, that nucleation evolves along the easiest of the available pathways, which in a given filament does not necessarily represent the entire statistical distribution.

A more quantitative analysis of that issue for RRAM devices goes beyond the scope of this paper. Here, we limit ourselves to pointing out that, based solely on the above statements, the variations between the parameters of the nominally identical RRAM structures should decrease with CF area. The latter prediction is in qualitative agreement with the observations presented in Fig. 4 of Ref. [2], where variations strongly increase with a CF resistance that is inversely proportional to the CF area. This aspect of the nanoglass behavior is similar to that discussed in the preceding section for random double-well potentials.

2. *Nucleation of insulating gap*

As explained in Sec. IV, the gap formation is triggered by the unfavorable polarization of a host material developed during the SET process. The gap constituting a new phase is energetically favorable, providing gain $Al\delta\mu_{\max}$ in free energy, where A is the gap cross-section area and l is its width. Here,

$$\delta\mu_{\max} \approx \delta\mu_1 + \delta\mu_2 \qquad (22)$$

corresponds to the transition from the unfavorably polarized CF to the insulating phase. We consider two possible

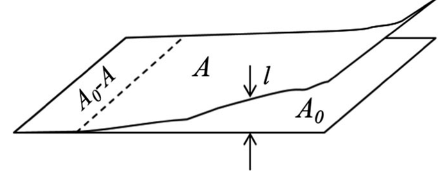

FIG. 5. Sketch of an insulating gap of area A and width l in the filament cross section of area A_0. Two edges are shown for the case of partial rupture where CF retains its integrity in the area $A_0 - A$.

scenarios: the complete rupture of CF, $A = A_0$, and the partial CF rupture leaving some neck of cross-section area $A_0 - A$ between the gap edges (Fig. 5), where A_0 is the cross-section area of CF before gap formation.

Complete rupture.—We assume first that the electronic processes remain fast enough to adiabatically follow changes in atomic configuration, particularly the electric current through the stack remaining the same due to the corresponding increase of the local electric field (the alternative case is discussed at the end of this subsection). The gap formation will then change the free energy by

$$F = -\delta\mu_{\max}A_0 l + 2A_0\sigma + \frac{E^2}{8\pi}\frac{\rho_i^2}{\rho_c^2}A_0 l. \qquad (23)$$

Here, $2\sigma A_0$ is the interfacial energy loss. The last term describes the electric-field energy due to the interior field E_{int} that must be, by a factor $\rho_i/\rho_c \gg 1$, stronger than $E = U/h$ to maintain the current flow through the stack. F becomes negative when

$$l \geq l_c = r_c\left(1 - \frac{E^2\rho_i^2}{8\pi\delta\mu_{\max}\rho_c^2}\right)^{-1}, \qquad (24)$$

where the classical nucleation radius $r_c = 2\sigma/\delta\mu_{\max}$ [56].

Once the gap is formed, the current will decrease by a factor of

$$I_D/I_E = \frac{\rho_i}{\rho_c}\left(1 - \frac{E^2\rho_i^2}{8\pi\delta\mu_{\max}\rho_c^2}\right), \qquad (25)$$

where I_D and I_E stand for the currents in points E and D in Fig. 1. Assuming the typical $E \sim 10^5$ V/cm and $\delta\mu_{\max} \sim 2\times 10^9$ J/m^3, one can estimate $E^2/8\pi\delta\mu_{\max} \sim 10^{-6}$, while the ratio ρ_i/ρ_c is sensitive to material properties and varies between different device recipes. (The voltage will change as well due to redistribution between the load and a just-formed gap resistance.)

It follows that (a) the snap-forward ratio I_D/I_E depends on the ratio of insulating and conductive phase resistivities varying between different materials, and (b) when the latter ratio is high enough, the filament breakup becomes impossible [I_D/I_E cannot be negative in Eq. (25)]: CF is stabilized by the electric field.

Partial rupture.—Following Fig. 5, the interior field $E_{\rm int}$ must be, by a factor $A_0/(A_0 - A)$, stronger than $E = U/l$ to provide continuous current flow through the gap. As a result, the free-energy change accompanying the gap formation becomes

$$F = -\delta\mu_{\rm max} Al + 2A\sigma + \frac{E^2}{8\pi}\frac{A_0^2}{(A_0 - A)^2} Al. \qquad (26)$$

F is stationary when

$$A_0 - A = A_0(E^2/8\pi\delta\mu_{\rm max})^{1/3} \quad (\ll A_0). \qquad (27)$$

The corresponding energy decrease must be greater than the surface energy loss $2\sigma A_0$. That takes place when $l > r_c$.

We observe that the insulating gap can nucleate with a width $l \gtrsim r_c$ nm, leaving a narrow bridging neck. As the gap is formed, the current will snap forward, decreasing by a factor of

$$I_D/I_E = A_0/(A_0 - A) = (8\pi\delta\mu_{\rm max}/E^2)^{1/3} \sim 100. \qquad (28)$$

The latter prediction is consistent with the data [2,4–7].

Comparing the free energies in Eqs. (23) and (26) shows that the complete gap rupture is energetically more favorable when $\rho_c/\rho_i < (E^2/8\pi\delta\mu_{\rm max})^{1/2} \sim 0.01$, where we use $E \sim 10^6$ V/cm and $\delta\mu_{\rm max} \sim 10^9$ J/m^3. (In the case of the very fast structural transition mentioned at the end of the preceding subsection, the latter inequality changes to $l/h < 0.01$.)

We end this section by pointing out its approximations lacking numerical factors and neglecting the concomitant thermal processes that may be significant [19]. However, this remains the only analytical approach to CF rupture phenomena since their first observation more than 100 years ago (for the contacts of dissimilar metals) [67]; further efforts are called upon.

B. Growth processes

Our approach is based on the reduction of a kinetic problem of the filament or gap growth to the free-energy analysis, which we briefly illustrated for the case of CF radii. We start with the kinetic Fokker-Planck equation, which, for the average CF radius (neglecting variations in an ensemble of different CFs) can be transformed into [68]

$$\frac{\partial r}{\partial t} = -b_r \frac{\partial F}{\partial r}. \qquad (29)$$

The latter has the standard meaning of a relation between the (growth) velocity and the (thermodynamic) force $-\partial F/\partial r$, with the mobility b_r. It follows that the steady-state average radius corresponds to the stationary point of the free energy, a condition that we use next.

We note that the concept of free energy F is not compromised by the power dissipation since the electric current is fixed by the circuit and serves only as a temperature source [68]. The corresponding requirement (of self-consistent Fokker-Planck equation) [69] is that the thermalization time τ_T must be shorter than that of the system evolution, empirically, $\tau_r \gtrsim 100$ ps [70]. In other words, the system remains quasistatic, with temperature adiabatically following its particular configurations.

For numerical estimates, we note that $\tau_T \sim L^2/\kappa$, where L is the characteristic linear dimension of the system and κ is the thermal diffusivity. The latter ratio of thermal conductivity [71] $\chi \sim 1$ W/m K over specific heat $c \sim 10$ J/cm^3 K is estimated as $\kappa \sim 10^{-3}$ cm^2/s. Assuming the nanometer-sized devices, $L \sim 1$ nm, then yields approximately 0.01 ns. Therefore, the existing RRAM devices fall in the domain $\tau_r \gtrsim \tau_T$, where the thermodynamic analysis applies at least semiquantitatively.

A particularly important case represents the thermalization process dominated by CF *per se* serving as the strongest heat conductor transferring energy to the device electrodes. In the case assumed earlier for the threshold switches [72] and modern RRAM devices [25],

$$\tau_T = h^2/\kappa, \qquad (30)$$

where κ is understood as the thermal diffusivity of Hf-based CF. Using the numerical values [25] $c \sim 2$ J/cm^3 K and $\chi \sim 0.2$ W/m K, it is estimated as $\kappa \sim 0.1$ cm^2/s, leading to $\tau_T \sim 10^{-12}$ s for a 10-nm-long CF, close to the estimate from the preceding paragraph. The difference is that Eq. (30) predicts the CF-length-dependent τ_T, which will result in a rather specific prediction of $V_{\rm SET}$ and CF resistance R independent of the h given in Sec. V B 1 below.

The major part of the free energy is given by

$$F = \int d^3 r c\delta T + 2\pi r h\sigma + \pi r^2 h\delta\mu + \int d^3 r \frac{E^2\varepsilon}{8\pi}. \qquad (31)$$

Here, c is the specific heat and δT is the temperature change. The first term in Eq. (31) represents the thermal contribution, the second and third correspond to the phase transformation, and the fourth stands for the electrostatic energy. We approximate the first terms with $\tau_T P$, where P is the Joule power produced by the filament.

1. Radial growth of CF

The domain *B-C* in Fig. 1 corresponds to the current source regime because the filament dynamic resistance $R \ll R_L$. The electrostatic energy does not change in the course of filament-radius growth and is neglected in what follows. Neglecting also the surface-tension term (see the discussion at the end of this subsection), the corresponding free energy can be written as

$$F = \tau_T I^2 R + \frac{\rho_c h^2 \delta\mu_1}{R}, \qquad (32)$$

where ρ_c is the resistivity of the CF phase and we use $R = \rho_c h/\pi r^2$. Optimizing the latter with respect to R yields its optimum value and the corresponding CF radius,

$$R^{(0)} \equiv \sqrt{\frac{\rho_c h^2 \delta\mu_1}{\tau_T I^2}}, \qquad r^{(0)} \equiv \left(\frac{\rho_c \tau_T}{\delta\mu_1}\right)^{1/4} \sqrt{\frac{I}{\pi}}. \qquad (33)$$

These results define the steady-state CF resistance and radius. The corresponding SET voltage is given by

$$U_{\mathrm{SET}} = R^{(0)} I = U_{\mathrm{SET}}^{(0)} \equiv h\sqrt{\frac{\rho_c \delta\mu_1}{\tau_T}}. \qquad (34)$$

A particularly important case of CF-dominated thermalization in Eq. (30) makes the CF resistance and the SET voltage independent of device thickness,

$$R^{(0)} = \sqrt{\frac{\rho_c \kappa \delta\mu_1}{I^2}}, \qquad r^{(0)} = \left(\frac{\rho_c h^2}{\kappa \delta\mu_1}\right)^{1/4} \sqrt{\frac{I}{\pi}}, \qquad (35)$$

and

$$U_{\mathrm{SET}}^{(0)} = \sqrt{\kappa \rho_c \delta\mu_1}. \qquad (36)$$

Equations (33) and (35) predict the dependence $R \propto I^{-1}$, explaining the observations in Table I. Also, using the above-estimated $\delta\mu_1 \sim 10^9$ J/m^3 and resistivity [25] $\rho_c \sim 10^{-4}$ Ωcm predicts the numerical values $R \approx 1$ kΩ, $r \approx 3$ nm, and $U_{\mathrm{SET}} \sim 0.1$ V consistent with the data [4].

Remarkably, Eqs. (33) and (35) predict CF resistance that is independent of device thickness h. The experimentally established fact of that independence, therefore, does not require a constriction described in the "hourglass" model [8,9] mentioned at the beginning of Sec. III above. [We should note, however, that, while Eqs. (33) and (35) show that the thickness-independent CF resistance can be understood without the assumptions about its determining constriction, they do not state that CF constrictions, such as those observed in Ref. [73], cannot exist.]

We note that the phenomenon $R \propto I^{-1}$ experimentally is not limited to RRAM and threshold-switching devices: it was observed for 1D granular metals [74,75] and, more than 100 years ago, for the granular media (metal filings) forming the coherer devices [76]. The approach presented here may be relevant for the latter two phenomena as well.

To make this subsection analysis more accurate, one can account for the above neglected surface-tension term as a perturbation. It can be conveniently estimated as $2\pi\sigma r h = \pi r^2 h \delta\mu (r_c/r)$, where $r_c = 2\sigma/\delta\mu$ is the classical nucleation radius [56] whose typical value in solids is on the order of 1 nm. The latter estimate shows that the surface term becomes significant when the filament radius remains small, $r \sim r_c$, but it can be neglected for the "grown" filament with $r \gg r_c$, which empirically corresponds to the vertical portion of the $B - C$ domain.

Adding the surface contribution to the free energy of Eq. (32) and optimizing it, to the accuracy of terms linear in σ, yields

$$R = R^{(0)}\left[1 + \frac{r_c}{4r^{(0)}}\right], \qquad U = U_{\mathrm{SET}}^{(0)}\left[1 + \frac{r_c}{4r^{(0)}}\right]. \qquad (37)$$

Taking into account that $r \propto \sqrt{I}$, we observe that the current-voltage characteristic becomes slightly "backslashed" (i.e., showing some negative slope), in qualitative agreement with the available data.

Finally, we note that combining Eqs. (35), (36), and (7) with $N_a = \pi r^2 h/a_0^3$ yields the relation between the SET process time τ and its driving current I (representing here the compliance current, i.e., the maximum current on the domain $B - C$ of Fig. 1 allowed by the setup),

$$\ln\left(\frac{\tau}{\tau_0}\right) = \frac{W_a}{\delta\mu_1 a_0^3 + kT_0}. \qquad (38)$$

The first term in the denominator describes the effect of the temperature increase $k\delta T$ and turns out to be independent of I. Its physical interpretation is that the Joule-heat-generated thermal-energy increase must be equal the chemical energy in order to overcome the energy deficit $\delta\mu_1$ per volume in Fig. 3. Another useful form of the latter result concerns the freezing temperature,

$$T_f = T_0 + \frac{a_0^3 \delta\mu_1}{k} = \frac{W_a}{\ln(\tau/\tau_0)}, \qquad (39)$$

and emphasizes its thermodynamic nature.

Using the above numerical values $a_0 = 0.2$ nm and $\delta\mu_1 = 10^9$ J/m^3 yields $\delta T \sim 600$ K. The latter falls in the ballpark of the earlier-measured and -modeled values of CF temperature [32,77–79].

As a final note, we mention that τ in Eq. (38) has the meaning of the characteristic time of radial-filament expansion, which exponentially decreases with the temperature T_f (and thus the heat per volume $\delta\mu_1$) necessary to maintain that process. Also, it should be remembered that Eqs. (38) and (39) are limited to the case of endothermic reaction (i.e., $\delta\mu_1 > 0$) where the relation $r \propto \sqrt{I}$ applies; it cannot be extended to the alternative case of $\delta\mu_1 > 0$.

2. Growth of insulating gap

Consider the opposite regime of voltage-source operations ($R \gg R_L$) corresponding to the RESET domain E-F in Fig. 1. As illustrated in Fig. 3, it is characterized by the change in chemical potential, $\delta\mu' = \mu_i - \mu_{\mathrm{mc}} = -\delta\mu_1 + \delta\mu_2 < 0$,

where the insulating gap is formed as a final product of the structural transformation involved. However, as explained in Sec. IV above and illustrated in Fig. 3, there is a significant difference in the transformation barriers, suggesting that the insulating gap is formed through the intermediate unstable state requiring an increase $\delta\mu_2 > 0$ in chemical potentials. After the energy $\delta\mu_2 \pi r^2 l$ is provided, the unstable CF quickly decays into the stable insulating phase. The free energy responsible for the former bottleneck process is described by

$$F = \frac{\tau_T U^2}{R_i} + \delta\mu_2 \pi r^2 l + \frac{E^2 \varepsilon}{8\pi} \pi r^2 l, \qquad (40)$$

where l stands for the gap width, and $R_i = \rho_i l/\pi r^2$ and ρ_i represent its resistance and resistivity.

The behavior of the electrostatic term in Eq. (40) depends on the relation between the gap-growth time t_g and the characteristic RC time of the system. Assuming $RC \ll t_g$, the system remains in equilibrium with the voltage source; hence, voltage U is given, and the field strength becomes U/l, yielding an electrostatic term that is inversely proportional to l, similar to the first term in Eq. (40). The electrostatic contribution decreases with l because maintaining constant voltage results in passing a charge through the voltage source [38]. (Specifically, $CU^2 \delta l/2l$ is the energy gain due to increase δl in the distance l between the plates of a parallel-plate capacitor C at a fixed voltage U.) Based on the experimental values [2], we assume here that $RC \ll t_g$.

With the above in mind, minimizing the free energy in Eq. (40) leads to the equation

$$-\frac{\tau_T U^2 \pi r^2}{\rho_i l^2} + \delta\mu_2 \pi r^2 + \frac{\varepsilon U^2 r^2}{8 l^2} = 0. \qquad (41)$$

Here, the first and third terms have similar l dependencies, and the latter is small for any practical choice of material parameters, for example, $\tau_T \sim 0.01$ ns, $\varepsilon \approx 25$ (for HfO_2 [80]) and $\rho_i \sim 0.001$–$0.1\ \Omega\,\mathrm{m}$.

Solving Eq. (41) yields the gap width l, its resistance R_i, and the current I that should be identified with the "saturation" current, $I_{R,\mathrm{sat}}$, marked in the Fig. 1 domain E-F,

$$l = \sqrt{\frac{\tau_T U^2}{\rho_i \delta\mu_2}} \quad \text{and} \quad I_{R,\mathrm{sat}} = \frac{U}{R_i} = r^2 \sqrt{\frac{\delta\mu_2}{\tau_T \rho_i}}. \qquad (42)$$

For numerical estimates, we assume $r \sim 10$ nm and $\rho_i \sim 100\rho_c \sim 10^{-2}\ \Omega$ m based on the typical difference in the *on*- and *off*-state resistances [81]. This choice of parameters yields a reasonable gap $l \sim 1$ nm and $I_{R,\mathrm{sat}} \sim 10\ \mu$A according to Eq. (42), in fair agreement with the data [2,82,83]. The sometime-observed deviations from the voltage-independent current in the domain E-F of Fig. 1 can be caused by the non-Ohmicity of the insulating phase resistivity.

Taking into account the discussion at the end of Sec. IV, Eq. (42) predicts that the saturation current, $I_{R,\mathrm{sat}}$, proportional to $\delta\mu_2$ should be time dependent. Such dependencies have been observed. For example, in the experimental design of Ref. [2], the time t that must be substituted in Eq. (13) is determined by the change in the electric potential divided by the voltage ramp rate $|dV/dt|$ leading to the observed dependence $I_{R,\mathrm{sat}}$ vs $|dV/dt|$.

For completeness, we mention an alternative RESET scenario where the domains E-F and $F-0$ overlap without hysteresis. One can consider indeed that, in spite of a certain increase in U^2, the increase in resistance at the E-F domain suppresses Joule heat enough to ensure that the freezing criterion in Eq. (7) obeys. Should that condition take place, the system would not structurally evolve in the domain E-F, resulting in the no-hysteresis behavior, and Eq. (42) becomes unapplicable.

Finally, we note that our above phenomenological theory is limited to the Ohmic mechanism of conductivity setting aside possibilities of electron tunneling [84–86] that would change the results in Eq. (42). Therefore, we would like to briefly describe the effects of quantum tunneling through the gap dielectric.

In our generic approach, we use the simplest expression, $R_T = R_T^0 \exp(l/a_T)$, for the tunneling resistance R_T vs gap width l, where R_T^0 and a_T are two phenomenological parameters. Using R_T instead of R_i and optimizing the free energy in Eq. (40) yields

$$l = a_T \ln\left(\frac{\tau_T U^2}{R_T^0 a_T \delta\mu_2 \pi r^2}\right) \quad \text{and} \quad I = \frac{a_T \delta\mu_2 \pi r^2}{\tau_T |U|}. \qquad (43)$$

We conclude that the gap logarithmically widens and the tunneling current decreases as $1/U$ with a voltage increase.

For numerical estimates, we assume $R_T^0 \sim 10\ \mathrm{k}\Omega$ (on the order of the quantum resistance [84–86]), $a_T \sim 1$ nm (typical of tunneling in solids), $r \sim 5$ nm, and the above-introduced $\tau_T \sim 0.01$ ns, $\delta\mu_2 \sim 10^9\ \mathrm{J/m^3}$. With the latter numbers, Eq. (43) yields $l \sim a_T \sim 1$ nm and $I \sim 10\ \mu$A for $|U| \sim 1$ V. It is worth noting that the latter quantum current is of an order of magnitude equal to $I_{R,\mathrm{sat}}$.

Because the tunneling contribution decreases, the Ohmic current will dominate starting at some voltage. A simple extrapolation of such a behavior takes the form

$$I = P1 + \frac{P2}{U}, \qquad (44)$$

where $P1$ and $P2$ are two parameters that can be determined from experiments and whose characteristic values are provided, respectively, in Eqs. (42) and (43).

TABLE III. Answering the questions in Table I.

Domain	Answer
A-B	Threshold voltage: Eq. (16).
B-C	SET voltage: Eq. (34).
C-0-*D*	Filament radius and resistance: Eq. (33)
D-E	$U_{\mathrm{RESET}} = -U_{\mathrm{SET}}$ and $I_{\mathrm{RESET}} = -I_{\mathrm{SET}}$, Eq. (28).
E-F	Expressions for $I_{R,\mathrm{sat}}$: Eq. (42)

VI. CONCLUSIONS

In this paper, we derive closed-form equations for all of the quantities listed in Table I.

Our results are summarized in Table III. The corresponding numerical estimates, while approximate, are in the vicinity of measured values.

The essence of our phenomenological theory is (a) the notion of the filament charging, (b) its accompanying polarization of the host material, and (c) the existence of three phase states of the material: stable insulating, unstable conducting, and long-lived metastable conducting. The items (a) and (b) are model independent, while (c) remains a model hypothesis, which, however, suffices to explain a large number of outstanding questions, as illustrated in Tables I and III.

Finally, our results contain a number of predictions calling upon experimental verification. Such is the phenomenon of filament charging, the temperature dependence of threshold voltage, the amplitude of the current snap forward, voltage dependence of the insulating gap width, and some others.

ACKNOWLEDGMENTS

This work was supported in part by the Semiconductor Research Corporation (SRC) under Contract No. 2016-LM-2654. We are grateful to D. A. Parshin for the useful discussions.

[1] J. C. Slonczewski, Current-driven excitation of magnetic multilayers, J. Magn. Magn. Mater. **159**, L1 (1996).

[2] A. Fantini, D. J. Wouters, R. Degraeve, L. Goux, L. Pantisano, G. Kar, Y.-Y. Chen, B. Govoreanu, J. A. Kittl, L. Altimime, and M. Jurczak, in *Proceedings of the 4th IEEE International Memory Workshop, Milan, 2012*, http://ieeexplore.ieee.org/document/6213646/.

[3] Y. Y. Chen, R. Degraeve, S. Clima, B. Govoreanu, L. Goux, A. Fantini, G. S. Kar, G. Pourtois, G. Groeseneken, D. J. Wouters, and M. Jurczak, in *Proceedings of the 2012 International Electron Devices Meeting (IEDM), San Francisco, 2012*, http://ieeexplore.ieee.org/abstract/document/6479079/.

[4] D. J. Wouters, L. Zhang, A. Fantini, R. Degraeve, L. Goux, Y. Y. Chen, B. Govoreanu, G. S. Kar, G. V. Groeseneken, and, and M. Jurczak, Analysis of complementary RRAM switching, IEEE Electron Device Lett. **33**, 1186 (2012).

[5] Z. Wei, K. Eriguchi, S. Muraoka, K. Katayama, R. Yasuhara, K. Kawai, Y. Ikeda, M. Yoshimura, Y. Hayakawa, K. Shimakawa, T. Mikawa, and S. Yoneda, in *Proceedings of the 2015 IEEE International Electron Devices Meeting (IEDM), Washington, DC, 2015* (IEEE, New York, 2015), p. 7.7.1.

[6] A. Sawa, T. Fujii, M. Kawasaki, and Y. Tokura, Colossal electro-resistance memory effect at metal/La_2CuO_4 interfaces, Jpn. J. Appl. Phys. **44**, L1241 (2005).

[7] A. Beck, J. G. Bednorz, Ch. Gerber, C. Rossel, and D. Widmer, Reproducible switching effect in thin oxide films for memory applications, Appl. Phys. Lett. **77**, 139 (2000).

[8] R. Degraeve, A. Fantini, N. Raghavan, L. Goux, S. Clima, Y. Y. Chen, A. Belmonte, S. Cosemans, B. Govoreanu, D. J. Wouters, Ph. Roussel, G. S. Kar, G. Groeseneken, and M. Jurczak, in *Proceedings of the 21th International Symposium on the Physical and Failure Analysis of Integrated Circuits (IPFA), Marina Bay Sands, Singapore, 2014*, http://ieeexplore.ieee.org/abstract/document/6898205/.

[9] K. M. Kim, M. H. Lee, G. H. Kim, S. J. Song, J. Y. Seok, J. H. Yoon, and C. S. Hwang, Understanding structure-property relationship of resistive switching oxide thin films using a conical filament model, Appl. Phys. Lett. **97**, 162912 (2010).

[10] U. Celano, L. Goux, A. Belmonte, K. Opsomer, A. Franquet, A. Schulze, C. Detavernier, O Richard, H. Bender, M. Jurczak, and W. Vandervorst, Three-dimensional observation of the conductive filament in nanoscaled resistive memory devices, Nano Lett. **14**, 2401 (2014).

[11] S. Privitera, G. Bersuker, B. Butcher, A. Kalantarian, S. Lombardo, C. Bongiorno, R. Geer, D. C. Gilmer, and P. D. Kirsch, Microscopy study of the conductive filament in HfO_2 resistive switching memory devices, Microelectron. Eng. **109**, 75 (2013).

[12] D. Halliday, R. Resnik, and J. Walker, *Fundamentals of Physics*, 10th ed. (Wiley, New York, 2014).

[13] J. Muller, P. Polakowski, S. Mueller, and T. Mikolajick, Ferroelectric hafnium oxide based materials and devices: Assessment of current status and future prospects, ECS J. Solid State Sci. Technol. **4**, N30 (2015).

[14] Y. Xu and J. D. Mackenzie, A theoretical explanation for ferroelectric-like properties of amorphous $Pb(Zr_xTi_{1-x})O_3$ and $BaTiO_3$, J. Non-Cryst. Solids **246**, 136 (1999).

[15] J. R. Jameson, W. Harrison, P. B. Griffin, and J. D. Plummer, Appl. Phys. Lett. **84**, 3489 (2004).

[16] X. Zhao and D. Vanderbilt, First-principles study of structural, vibrational, and lattice dielectric properties of hafnium oxide, Phys. Rev. B **65**, 233106 (2002).

[17] A. K. T. Assis and J. A. Hernandes, *The Electric Force of a Current: Weber and the Surface Charges of Resistive Conductors Carrying Steady Currents* (Apeiron, Montreal, 2007).

[18] I. E. Irodov, *Basic Laws of Electromagnetism* (G.K. Publications, New Dehli, 2016).

[19] A. A. Sharma, I. V. Karpov, R. Kotlyar, and J. Kwon, Dynamics of electroforming in binary metal oxide-based resistive switching memory, J. Appl. Phys. **118**, 114903 (2015).

[20] M. L. C. Cooray and V. G. Karpov, Long range fluctuations in thin-film structures, Phys. Rev. B **75**, 155303 (2007).
[21] J. C. Maxwell, in *Scientific Papers*, edited by W. D. Niven (Dover, New York, 1965), Vol. II, p. 672.
[22] K. T. McDonald, Capacitance of a thin conducting disk, and of conducting spheroids, http://physics.princeton.edu/~mcdonald/examples/index.html.
[23] R. W. Scharstein, Capacitance of a tube, J. Electrost. **65**, 21 (2007).
[24] V. N. Kruchinin, V.Sh. Aliev, T. V. Perevalov, D. R. Islamov, V. A. Gritsenko, I. P. Prosvirin, C. H. Cheng, and A. Chin, Nanoscale potential fluctuation in non-stoichiometric HfO_x and low resistive transport in RRAM, Microelectron. Eng. **147**, 165 (2015).
[25] D. Ielmini, Modeling the universal SET/RESET characteristics of bipolar RRAM by field- and temperature-driven filament growth, IEEE Trans. Electron Devices **58**, 4309 (2011).
[26] C. T. Moynihan, A. J. Easteal, and J. Wilder, Dependence of the glass transition temperature on heating and cooling rate, J. Phys. Chem. **78**, 2673 (1974).
[27] S. B. Aldabergenova, N. A. Feoktistov, V. G. Karpov, K. V. Koughia, A. B. Pevtsov, and V. U. Solovijev, in *Transport, Correlation and Structural Defects*, edited by H. Fritzsche, Advances in Disordered Semiconductors Vol. 3 (World Scientific, Singapore, 1990), p. 129.
[28] R. A. Street, *Hydrogenated Amorphous Silicon* (Cambridge University Press, New York, 1991).
[29] N. Ciocchini, M. Laudato, M. Boniardi, E. Varesi, P. Fantini, A. L. Lacaita, and D. Ielmini, Bipolar switching in chalcogenide phase change memory, Sci. Rep. **6**, 29162 (2016).
[30] M. Maestro, J. Martin-Martinez, J. Diaz, A. Crespo-Yepes, M. B. Gonzalez, R. Rodriguez, F. Campabadal, M. Nafria, and X. Aymerich, Analysis of SET and RESET mechanism in Ni/HfO_2-based RRAM with fast ramped voltages, Microelectron. Eng. **147**, 176 (2015).
[31] C. Schindler, G. Staikov, and R. Waser, Electrode kinetics of $Cu\text{-}SiO_2$-based resistive switching cells: Overcoming the voltage-time dilemma of electrochemical metallization memories, Appl. Phys. Lett. **94**, 072109 (2009).
[32] E. Yalon, A. A. Sharma, M. Skowronski, J. A. Bain, D. Ritter, and I. V. Karpov, Thermometry of filamentary RRAM devices, IEEE Trans. Electron Devices **62**, 2972 (2015).
[33] D. Erdemir, A. Y. Lee, and A. S. Meyerson, Nucleation of crystals from solution: Classical and two-step models, Acc. Chem. Res. **42**, 621 (2009).
[34] B. Govoreanu, A. Ajaykumar, H. Lipowicz, Y. Y. Chen, J. C. Liu, R. Degraeve, L. Zhang, S. Clima, L. Goux, I. P. Radu, A. Fantini, N. Raghavan, G. S. Kar, W. Kim, A. Redolfi, D. J. Wouters, L. Altimime, and M. Jurczak, in *Proceedings of the 5th IEEE International Memory Workshop, Monterey, 2013*, http://ieeexplore.ieee.org/abstract/document/6582095/.
[35] J. Park, E. Cha, I. Karpov, and H. Hwang, Dynamics of electroforming and electrically driven insulator-metal transition in NbO_x selector, Appl. Phys. Lett. **108**, 232101 (2016).
[36] L. D. Landau and E. M. Lifsitz, *Statistical Physics* (Pergamon, Oxford, 1980).
[37] E. Yalon, A. Gavrilov, S. Cohen, and D. Ritter, Validation and extension of local temperature evaluation of conductive filaments in RRAM devices, IEEE Trans. Electron Devices **62**, 3671 (2015).
[38] L. D. Landau and E. M. Lifsitz, *Electrodynamics of Continuous Media* (Pergamon, Oxford, 1984).
[39] S. Meister, S.-B. Kim, J. J. Cha, H.-S. P. Wong, and Y. Cui, *In situ* transmission electron microscopy observation of nanostructural changes in phase-change memory, ACS Nano **5**, 2742 (2011).
[40] I. V. Karpov, M. Mitra, D. Kau, G. Spadini, Y. A. Kryukov, and V. G. Karpov, Fundamental drift of parameters in chalcogenide phase change memory, J. Appl. Phys. **102**, 124503 (2007).
[41] S. Ambrogio, S. Balatti, V. McCaffrey, D. C. Wang, and D. Ielmini, Noise-induced resistance broadening in resistive switching memory—Part I: Intrinsic cell behavior, IEEE Trans. Electron Devices **62**, 3805 (2015).
[42] Sh. Kogan, *Electronic Noise and Fluctuations in Solids* (Cambridge University Press, Cambridge, England, 1996).
[43] F. N. Hooge and P. A. Bobbert, On the correlation function of $1/f$ noise, Physica (Amsterdam) **239B**, 223 (1997).
[44] A. Fantini, G. Gorine, R. Degraeve, L. Goux, C. Y. Chen, A. Redolfi, S. Clima, A. Cabrini, G. Torelli, and M. Jurczak, in *Proceedings of the 2015 International Electron Devices Meeting (IEDM), Washington, DC, 2015*, http://ieeexplore.ieee.org/abstract/document/7409648/.
[45] S. Ambrogio, S. Balatti, A. Cubeta, A. Calderoni, N. Ramaswamy, and D. Ielmini, Statistical fluctuations in HfO_x resistive-switching memory—Part II: Random telegraph noise, IEEE Trans. Electron Devices **61**, 2920 (2014).
[46] M. Maestro, J. Diaz, A. Crespo-Yepes, M. B. Gonzalez, J. Martin-Martinez, R. Rodriguez, M. Nafria, F. Campabadal, and X. Aymerich, New high resolution random telegraph noise (RTN) characterization method for resistive RAM, Solid State Electron. **115**, 140 (2016).
[47] M. J. Kirton and M. J. Uren, Noise in solid-state microstructures: A new perspective on individual defects, interface states and low-frequency $1/f$ noise, Adv. Phys. **38**, 367 (1989).
[48] Shih-Chang Tsai, San-Lein Wu, Jone-Fang Chen, Kai-Shiang Tsai, Tsung-Hsien Kao, Chih-Wei Yang, Cheng-Guo Chen, Kun-Yuan Lo, Osbert Cheng, Yean-Kuen Fang, and Shoou-Jinn Chang, Investigation of low-frequency noise characterization of 28-nm high-k pMOSFET with embedded SiGe source/drain, J. Nanomater. **2014**, 787132 (2014).
[49] V. G. Karpov, Fluctuations in the thermal expansion of disordered systems, Pis'ma Zh. Eksp. Teor. Fiz. **55**, 59 (1992) [Sov. Phys. JETP Lett. **55**, 60 (1992)].
[50] C. Y. Chen, A. Fantini, L. Goux, G. Gorine, A. Redolfi, G. Groeseneken, and M. Jurczak, Novel flexible and cost-effective retention assessment method for TMO-based RRAM, IEEE Electron Device Lett. **37**, 1112 (2016).
[51] V. G. Karpov, Y. A. Kryukov, I. V. Karpov, and M. Mitra, Field induced nucleation in glasses, Phys. Rev. B **78**, 052201 (2008).
[52] I. V. Karpov, M. Mitra, D. Kau, G. Spadini, Y. A. Kryukov, and V. G. Karpov, Evidence of field induced nucleation in phase change memory, Appl. Phys. Lett. **92**, 173501 (2008).

[53] V. G. Karpov, Y. A. Kryukov, I. V. Karpov, and M. Mitra, Crystal nucleation in phase change memory, J. Appl. Phys. **104**, 054507 (2008).

[54] M. Nardone, V. G. Karpov, C. Jackson, and I. V. Karpov, Unified model of nucleation switching, Appl. Phys. Lett. **94**, 103509 (2009).

[55] V. G. Karpov, R. E. E. Maltby, I. V. Karpov, and E. Yalon, Field-Induced Nucleation in the Presence of a Metal Electrode, Phys. Rev. Applied **3**, 044004 (2015).

[56] D. Kaschiev, *Nucleation: Basic Theory with Applications* (Butterworth-Heinemann, Oxford, 2000).

[57] L. Cormier, Nucleation in glasses—New experimental findings and recent theories, Procedia Mater. Sci. **7**, 60 (2014).

[58] J. A. Kalb, C. Y. Wen, F. Spaepenb, H. Dieker, and M. Wuttig, Crystal morphology and nucleation in thin films of amorphous Te alloys used for phase change recording, J. Appl. Phys. **98**, 054902 (2005).

[59] C. Barrett, W. Nix, and A. Tetelman, *The Principles of Engineering Materials* (Prentice-Hall, Englewood Cliffs, NJ, 1973).

[60] C. Weinberg and G. F. Nelson, On the possibility of critical radius measurements in the homogeneous crystal nucleation of glass, J. Non-Cryst. Solids **74**, 177 (1985).

[61] P. M. Valov and V. I. Leiman, Size distribution of CuCl nanoparticles in glass in various stages of nucleation, Phys. Solid State **51**, 1703 (2009).

[62] H. Hermann, N. Mattern, S. Roth, and P. Uebele, Simulation of crystallization processes in amorphous iron-based alloys, Phys. Rev. B **56**, 13888 (1997).

[63] D. P. Paul, A. Thamizhavel, and C. Subramanian, Determination of nucleation parameters of YBCO from high temperature solution, Cryst. Res. Technol. **34**, 503 (1999).

[64] M. C. Weinberg, E. D. Zanotto, and S. Manrich, Classical nucleation theory with a size dependent interfacial tension: $Li_2O_2SiO_2$ crystal nucleation, Phys. Chem. Glasses **33**, 99 (1992).

[65] V. M. Yurov, S. A. Guchenko, and M. S. Gyngazova, Effect of an electric field on nucleation and growth of crystals, IOP Conf. Ser.: Mater. Sci. Eng. **110**, 012019 (2016).

[66] A. Fantini, L. Goux, R. Degraeve, D. J. Wouters, N. Raghavan, G. Kar, A. Belmonte, Y. Y. Chen, B. Govoreanu, and M. Jurczak, Intrinsic Switching Variability in HfO_2 RRAM, in *Proceedings of the 5th IEEE International Memory Workshop, Monterey, 2013* (IEEE, New York, 2013), p. 30.

[67] R. H. Goddard, On the conduction of electricity at contacts of dissimilar metals, Phys. Rev. **34**, 423 (1912).

[68] V. G. Karpov, M. Nardone, and M. Simon, Thermodynamics of second phase conductive filaments, J. Appl. Phys. **109**, 114507 (2011).

[69] S. Nayakshin and F. Mela, Self-consistent Fokker-Planck treatment of particle distributions in astrophysical plasmas, Astrophys. J. Suppl. Ser. **114**, 269 (1998).

[70] A. C. Torrezan, J. P. Strachan, G. Medeiros-Ribeiro, and R. S. Williams, Sub-nanosecond switching of a tantalum oxide memristor, Nanotechnology **22**, 485203 (2011).

[71] M. A. Panzer, M. Shandalov, J. A. Rowlette, Y. Oshima, Y. W. Chen, P. C. McIntyre, and K. E. Goodson, Thermal properties of ultrathin hafnium oxide gate dielectric films, IEEE Electron Device Lett. **30**, 1269 (2009).

[72] K. E. Petersen and D. Adler, State of amorphous threshold switches, J. Appl. Phys. **47**, 256 (1976).

[73] E. Yalon, E. I. Karpov, V. Karpov, I. Ries, D. Kalaev, and D. T. Ritter, Detection of the insulating gap and conductive filament growth direction in resistive memories, Nanoscale **7**, 15434 (2015).

[74] E. Falcon, B. Castaing, and M. Creyssels, Nonlinear electrical conductivity in a 1D granular medium, Eur. Phys. J. B **38**, 475 (2004).

[75] P. Béquin and V. Tournat, Electrical conduction and Joule effect in one-dimensional chains of metallic beads: Hysteresis under cycling DC currents and influence of electromagnetic pulses, Granular Matter **12**, 375 (2010).

[76] K. E. Guthe, On the action of the coherer, Phys. Rev. **12**, 245 (1901); K. E. Guthe and A. Trowbridge, On the theory of the coherer, Phys. Rev. **11**, 22 (1900).

[77] S. Kim, S.-J. Kim, K. M. Kim, S. R. Lee, M. Chang, E. Cho, Y.-B. Kim, C. J. Kim, U.-In Chung, and In-K. Yoo, Physical electro-thermal model of resistive switching in bi-layered resistance-change memory, Sci. Rep. **3**, 1680 (2013).

[78] E. Yalon, I. Riess, and D. Ritter, Heat dissipation in resistive switching devices: Comparison of thermal simulations and experimental results, IEEE Trans. Electron Devices **61**, 1137 (2014).

[79] D. Niraula and V. G. Karpov, Heat transfer in filamentary RRAM devices, IEEE Trans. Electron Devices, DOI: 10.1109/TED.2017.2741782 (2017).

[80] A. P. Huang, Z. C. Yang, and P. K. Chu, in *Advances in Solid State Circuits Technologies*, edited by Paul K. Chu (InTech, Rijeka, Croatia, 2010), p. 333.

[81] E. Hildebrandt, J. Kurian, M. M. Muller, T. Schroeder, H.-J. Kleebe, and L. Alff, Controlled oxygen vacancy p-type conductivity in $HfO2_x$ thin films, Appl. Phys. Lett. **99**, 112902 (2011).

[82] H. Y. Lee, Y. S. Chen, P. S. Chen, T. Y. Wu, F. Chen, C. C. Wang, P. J. Tzeng, M.-J. Tsai, and C. Lien, Low-power and nanosecond switching in robust hafnium oxide resistive memory with a thin Ti cap, IEEE Electron Device Lett. **31**, 44 (2010).

[83] A. Kalantarian, G. Bersuker, D. C. Gilmer, D. Veksler, B. Butcher, A. Padovani, O. Pirrotta, L. Larcher, R. Geer, and Y. Nishi, in *Proceedings of the IEEE International Reliability Physics Symposium (IRPS), Anaheim, 2012* (IEEE, New York, 2012), p. 6C.4.1.

[84] S. Long, X. Lian, C. Cagli, X. Cartoixà, R. Rurali, E. Miranda, D. Jiménez, L. Perniola, M. Liu, and J. Suñé, Quantum-size effects in hafnium-oxide resistive switching, Appl. Phys. Lett. **102**, 183505 (2013).

[85] H. Lv, X. Xu, P. Sun, H. Liu, Q. Luo, Q. Liu, W. Banerjee, H. Sun, S. Long, L. Li, and M. Liu, Atomic view of filament growth in electrochemical memristive elements, Sci. Rep. **5**, 13311 (2015).

[86] Y. Li, S. Long, Y. Liu, C. Hu, J. Teng, Q. Liu, H. Lv, J. Su, and M. Liu, Conductance quantization in resistive random access memory, Nanoscale Res. Lett. **10**, 420 (2015).